axioms

MDPI

Article

A Study Using the Network Simulation Method and Nondimensionalization of the Fiber Fuse Effect

Juan Francisco Sanchez-Pérez [1,*], Joaquín Solano-Ramírez [2], Fulgencio Marín-García [3] and Enrique Castro [1]

[1] Department of Applied Physics and Naval Technology, Universidad Politécnica de Cartagena (UPCT), Campus Muralla del Mar, 30202 Cartagena, Spain; enrique.castro@upct.es
[2] Department of Mechanical Engineering, Materials and Manufacturing, Universidad Politécnica de Cartagena (UPCT), Campus Muralla del Mar, 30202 Cartagena, Spain; joaquin.solano@upct.es
[3] Department of Automation Engineering, Electrical Engineering and Electronic Technology, Universidad Politécnica de Cartagena (UPCT), Campus Muralla del Mar, 30202 Cartagena, Spain; pentxo.marin@upct.es
* Correspondence: juanf.sanchez@upct.es

Abstract: This paper presents an innovative approach to modelling the fiber optic fusion effect using the Network Simulation Method (NSM). An analogy between the heat conduction equations and electrical circuits is developed, allowing a complex physical problem to be transformed into an equivalent electrical system. Using NGSpice, thermal interactions in an anisotropic optical fiber under high optical power conditions are simulated. The methodology addresses the distribution of the temperature in the system, considering thermal variations and temperature-dependent material characteristics. In an NSM equivalent circuit, the effect of applying the spark is modelled by a switch that switches the spark-generating source on and off. It can be seen that temperature variation with time, or temperature rise rate (K/s), depends on the applied power. In addition, the mathematical method of nondimensionalization is used to study the real influence of each parameter of the problem on the solution and the relationship between the variables. Four optical fiber cases are analysed, each characterised by different areas and refractive indices, revealing how these variables affect the propagation of the melting phenomenon. The results highlight the effectiveness of the NSM in solving nonlinear and coupled problems in thermal engineering, providing a solid framework for future research in the optimisation of optical communication systems.

Keywords: network simulation method; mathematical modelling; non-linear material characteristics; coupled differential equations; nondimensionalization; heat transfer

MSC: 76M55; 80M10; 37N30

check for updates

Academic Editor: Giovanni Nastasi

Received: 21 November 2024
Revised: 20 December 2024
Accepted: 23 December 2024
Published: 26 December 2024

Citation: Sanchez-Pérez, J.F.; Solano-Ramírez, J.; Marín-García, F.; Castro, E. A Study Using the Network Simulation Method and Nondimensionalization of the Fiber Fuse Effect. *Axioms* **2025**, *14*, 2. https://doi.org/10.3390/axioms14010002

1. Introduction

The fiber fusion effect, also known as optical discharge, refers to a phenomenon that takes place in fiber optic cables when high-density radiation is transmitted. This process involves an initial stage of optical breakdown, which is succeeded by a plasma spark that moves along the fiber towards the source of radiation, causing significant damage to large portions of the fiber optic lines (see Figure 1). This effect was initially explained by Blow et al. during the years 1987–1988 [1–3]. A more detailed description of the problem, as well as the properties used to solve it, can be found in the article by Starikova et al. [4].

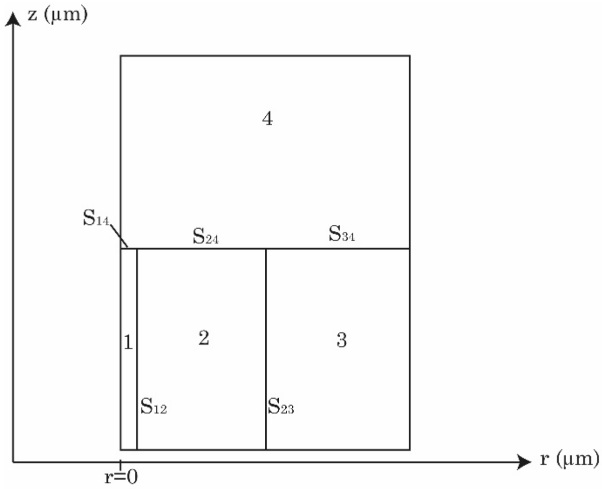

Figure 1. The computational space is integrated by four distinct regions with varying thermophysical characteristics: the core (1), the cladding (2), the guard envelope (3), and the metal plate (4). Thermal equilibrium is maintained at the interfaces between these regions.

In the book *Fiber Fuse*, Todoroki, S. [5] describes the phenomenon of fiber fusion, which causes a serious problem for current optical communication systems. High-power light often causes catastrophic damage to optical devices. When the fiber melts, a heated region of the fiber cable emits a few watts of light and travels towards the light source, destroying its core region. The book includes the classification of its propagation mode and the self-pulse effect.

Due to the drastic consequences of this phenomenon, it has been studied and analysed by several researchers. Ha, W et al. [6] examine the non-linear fiber fusion effect (FFE) in hollow optical fibers (HOF), which feature a central void encircled by a ring core with a high refractive index, along with a silica outer layer, in contrast to traditional solid-core fibers. They provide thorough comparisons regarding threshold power, the formation of holes, and penetration depth.

In the study conducted by Shuto, Y. [7], the focus is on understanding how core melting and fiber melting occurs in a single-mode fiber optic connector. The process of heat flow in the core, which leads to the melting of the fiber core, is evaluated using the explicit finite difference method. Meanwhile, Xiao et al. [8] explore the conditions that trigger fiber fusion (IFF), a severe type of damage that impacts all optical fibers, particularly those made of silica. An analysis of fibers with various chemical compositions is performed prior to IFF, revealing for the first time a consistent relationship between critical temperatures and the optical powers they transmit.

The work of Konin et al. [9] studies and analyses the internal structure of microcavities in single-mode and multimode acrylate and polyimide-coated optical fibers, which appear due to the melting that occurs when a plasma spark propagates through the core. The study is carried out on the structure of the microcavities on the outer and lateral surfaces of the fibers.

Shuto, Y. [10] examines the impact of fiber melting in multicore fibers (MCF) through the explicit finite difference method, utilising a thermochemical model for SiOx production. The analysis presumes that MCF varieties possess a uniform refractive index profile akin to that found in doubly coated single-mode fibers. This study is influenced by the presence of optical power restrictions caused by the fiber melting effect and the limited transmission bandwidth set by fiber optic amplifiers.

In order to complete the state of the art of the problem addressed in this article, we can highlight a series of references that may be useful when it comes to deepening the knowledge of the fiber fuse phenomenon [8,11–13], as well as being able to clearly see some of the industrial applications that have been made using this effect [14–16].

This article wants to contribute to the analysis of the fiber fusion effect by using a new approach to modelling it with the NSM. So, the numerical model of the optical breakdown starting process in the fiber and the thermophysical characteristics of optical fibers are shown. Subsequently, the equivalent formulation of the physical problem in the SNM will be presented. With the results obtained, the initial phenomenon, as well as the propagation of this defect, can be better understood.

To solve the model, the NSM has been used. This is a numerical simulation method, which is a widely tested method, by Peusner, L., Nagel, L. and Nagel, L. [17–19]. In this method, the equations defining the physical problem are transformed into electrical circuits, with a behaviour in their response equivalent to the physical equations.

The open-source program NGSpice has been used to solve the different circuits that make up the equivalent problem. NGSpice provides the numerical solutions to the problem, and by means of the inverse path to the one used to transform the original problem, the solutions to the physical problem can be obtained, and in this way, conclusions can be drawn about the results.

Furthermore, the nondimensionalisation numerical procedure makes it possible to determine the influence of each study variable of the problem by grouping them into monomials. This technique has been used in several engineering problems, Sánchez-Pérez et al. [20].

This paper presents a model based on the heat transfer equation in the initial stage of fiber fusion. With this model, the temperature distribution is obtained in the same, in the stationary phase, neglecting the transient. With this model, the temperature distribution in the same, in the transient phase and studying certain cases is obtained. The plasma spark process movement is neglectable. The calculations were performed using NGSpice V42 and Matlab R2020. In addition, the study of nondimensionalization is indicated for the study of the influence of the variables.

2. Materials and Methods

This research investigates an anisotropic optical fiber with cylindrical geometry. A cylindrical coordinate system is employed for modelling, with the z-axis aligned with the fiber's axis and the r-axis along its span. The computational space, depicted in Figure 1, is axisymmetric, allowing for 2D analysis in the z-r plane. Symmetry conditions are applied at the axis of symmetry (r = 0). The distribution of temperature does not depend on the polar angle. The computational domain illustrated in Figure 1 is made up of four elements, each exhibiting distinct thermophysical characteristics. The conditions for thermal equilibrium are satisfied at the boundaries between these elements.

A single-mode fiber (SMF-28e) with a stepped refractive index profile is examined. The fiber is pressed against a duraluminum plate, and the starting temperature of both is T_0 = 293 K.

The material properties of the fiber are obtained from SMF-28e specifications, while the duraluminum plate adheres to ISO standard 2024. Table 1 provides a summary of the materials and dimensions of each region.

Table 1. Values for the different simulation cases [4].

Case	λ, nm	n_1	n_2	V	A_{eff}, μm^2
1	1080	1.4483	1.4439	2.76	13.25
2	1310	1.4552	1.4508	2.17	15.29
3	1550	1.4617	1.4573	1.88	17.27
4	2050	1.4662	1.4618	1.39	23.49

The core of the fiber (1), its cladding (2), the protective reinforcement cladding (3), and the metal plate (4) in Figure 1 have contact contours with each other at S_{12}, S_{14}, S_{23}, S_{24}, and S_{34}.

The distribution of the temperature T(r,z,t) within the computational domain is ruled by the heat conduction expression as follows:

$$\rho_i C_{p_i}\frac{\partial T}{\partial t} = k_i\left(\frac{\partial^2 T}{\partial r^2} + \frac{1}{r}\frac{\partial T}{\partial r} + \frac{\partial^2 T}{\partial z^2}\right) + Q \tag{1}$$

where i = 1–4 is the section number (Figure 1), ρ_i are the densities $(\mathrm{kg/m^3})$, C_{p_i} are the specific heat capacities (J/(kg K)), k_i is the thermal conductivity of the materials (W/(mK)), and Q is the heat source, whose intensity is obtained by optical radiation ($\mathrm{W/m^3}$). In the article [4], the authors show temperature-dependent functions.

Assuming that the temperature changes across the interface continuously, at edges S_{12}, S_{14}, S_{23}, S_{24}, and S_{34} of the calculation scheme, the heat flow equilibrium conditions apply:

$$\left(k_i\frac{\partial T}{\partial r}l_r + k_i\frac{\partial T}{\partial z}l_z\right)_{S_{ij}} = \left(k_j\frac{\partial T}{\partial r}l_r + k_j\frac{\partial T}{\partial z}l_z\right)_{S_{ij}} \tag{2}$$

where l_r and l_z are the unit vector projections onto the r and z axes. The outer contour is considered to be quite well conducting with T_0 = 293 K.

The heat source, Q, is determined by:

$$Q(r,z) = \alpha(r,\ z)\frac{P}{A_{eff}}\Gamma(r,z) \tag{3}$$

where $\alpha(r,\ z)$ is equal to the aggregation of the under normal conditions absorption coefficient α_0 and the electron gas absorption coefficient α_e. describes the non-linear absorption of radiation in chaotically localised defects in the fiber. Defects appear in the fiber core because of chemical reactions in fabrication, as shown by Carslow, H.S. et al. and Davis et al. [21,22]. P is the input power (W), Γ is the normalised Gaussian distribution $\Gamma(\mathrm{x}) = \frac{1}{\sqrt{2\pi}}e^{-\frac{x^2}{2}}$ and A_{eff} is the effective area of the mode point (m^2). Γ takes a two-dimensional form due to the solution is a two-dimensional layer:

$$\Gamma(r,z) = \Gamma(r)\cdot\Gamma(z) \tag{4}$$

In the article [23], the GeE′ concentration ions are obtained by:

$$n_{GeE'} = n_p e^{-\frac{E_f}{k_B T}} \tag{5}$$

where $E_f = 2.5$ eV is the GeE′ formation energy, $n_p = 1.72 \times 10^{15}\ \mathrm{m}^{-3}$ is the GeE′ centre concentration at 293 K, and k_B is the Boltzmann constant. The quartz, due to free electrons conductivity, will be stated by:

$$\sigma = e\mu_e n_e = e\mu_e n_p e^{-\frac{E_f}{k_B T}} \tag{6}$$

where e is the modulus of charge of the electrons, μ_e is the electron drift velocity, with $5 \times 10^{-3}\mathrm{m}^2/(\mathrm{V{\cdot}s})$ [24], and $n_e = n_{GeE\prime}$. Considering (5) the electron gas absorption coefficient in the fiber, Equation (3), will equal to this expression:

$$\alpha_e = \frac{k_B n_1}{\sqrt{2}} \left[\sqrt{1 + \left(\frac{\mu_0 c_0 \sigma}{k_0 n_1^2} \right)^2} - 1 \right]^{\frac{1}{2}} \approx \frac{\mu_0 c_0 \sigma}{2n_1} = \frac{\mu_0 c_0}{2n_1} e\mu_e n_p e^{-\frac{E_f}{k_B T}} \tag{7}$$

where n_1 is the refractive index at the core, μ_0 is the magnetic permeability, c_0 is the vacuum speed of light and k_0 is the vacuum wavenumber.

The effective area of the model in Equation (3) is solved employing the effective radius for each of the wavelengths, Marcuse et al. [25]

$$A_{eff} = \pi a^2 \left(0.65 + \frac{1.619}{V^{\frac{3}{2}}} + \frac{2.879}{V^6} \right)^2 \tag{8}$$

where a is the fiber core radius (see Table 1). The parameter V is the normalised frequency [4]:

$$V = \frac{2\pi a}{\lambda} \sqrt{n_1^2 - n_2^2} \tag{9}$$

where λ is the transported radiation wavelength, n_2 is the fiber cladding refractive index.

Finally, in Table 1, Starikova, V. A. et al. [4] presents different values of wavelength, core refractive index, cladding refractive index and area to simulate different cases with the NSM and in Table 2, Starikova, V. A. et al. [4] gives some values of the different parameters that appear in the equations that make up the mathematical model.

Table 2. Values of the constants for the calculation model [4].

Description	Value	Units
Boltzmann's constant	$1.38{\cdot}10^{-23}$	J/K
Core refractive index	1.4617	
Charge of electron	$1.6{\cdot}10^{-19}$	C
Concentration	$1.72{\cdot}10^{15}$	m^{-3}
Input power	1.10	W
Formation energy GeE0	$4.0054{\cdot}10^{-19}$	J
Light velocity	$3{\cdot}10^{8}$	m/s
Core radius	$4.1{\cdot}10^{-6}$	m
Core layer thickness	$4.1{\cdot}10^{-6}$	m
Magnetic constant	$1.2566{\cdot}10^{-6}$	H/m
Drift mobility of electrons	$5{\cdot}10^{-3}$	$\mathrm{m}^2/(\mathrm{V{\cdot}s})$

2.1. Mathematical Model of the Heat Transfer Mechanism

The mathematical model we will discuss pertains to a cylindrical structure composed of potentially diverse materials whose properties are subject to temperature variations, as outlined by Fernández-García, M. et al. [26].

As previously mentioned, the model incorporates heat transfer mechanisms.

For conduction processes, Fourier's law is employed to quantify heat transfer:

$$\alpha \left(\frac{\partial^2 T}{\partial x^2} + \frac{\partial^2 T}{\partial y^2} + \frac{\partial^2 T}{\partial z^2} \right) + \frac{Q}{\rho c_e} = \frac{\partial T}{\partial t}\, ; \alpha = \frac{k}{\rho c_e} \tag{10}$$

In the equation above, T represents temperature (K), α is thermal diffusivity (m^2/s), k is thermal conductivity (W/mK), c_e is specific heat capacity (J/kg K), ρ is density (kg/m^3), t is time (s), and x, y, and z are spatial coordinates. As stated earlier, thermal conductivity, density, specific heat, and, consequently, thermal diffusivity will be declared as temperature functions.

Given the cylindrical geometry of the problem, it is advantageous to formulate it in cylindrical coordinates. The angle, φ; the radius, r; and the height, z, define the equation illustrated in Figure 2:

$$\frac{1}{r}\frac{\partial}{\partial r}\left(k\,r\frac{\partial T}{\partial r}\right)+\frac{1}{r^2}\frac{\partial}{\partial \varphi}\left(k\,\frac{\partial T}{\partial \varphi}\right)+\frac{\partial}{\partial z}\left(k\frac{\partial T}{\partial z}\right)+Q=\rho c_e\frac{\partial T}{\partial t} \tag{11}$$

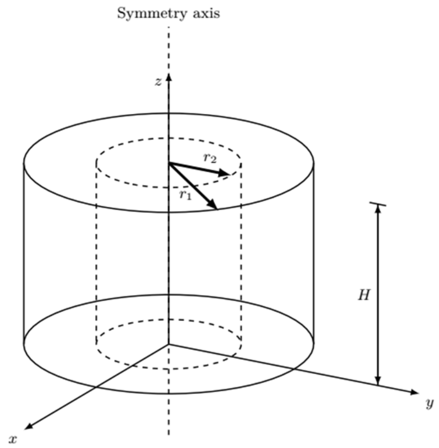

Figure 2. Cylindrical geometry.

It can be simplified, because of the symmetry of the problem, to two dimensions, axial and radial, leaving Equation (11) as follows:

$$\frac{1}{r}\frac{\partial}{\partial r}\left(k\,r\frac{\partial T}{\partial r}\right)+\frac{\partial}{\partial z}\left(k\frac{\partial T}{\partial z}\right)+Q=\rho c_e\frac{\partial T}{\partial t} \tag{12}$$

It is obtained the following, if it is developed the above expression:

$$\frac{1}{r}\frac{k}{\rho c_e}\frac{\partial T}{\partial r}+\frac{k}{\rho c_e}\frac{\partial^2 T}{\partial r^2}+\frac{k}{\rho c_e}\frac{\partial^2 T}{\partial z^2}+\frac{Q}{\rho c_e}=\frac{\partial T}{\partial t} \tag{13}$$

Grouping the properties together streamlines their integration into the network model. This is particularly beneficial considering their temperature-dependent nature.

To account for convective heat transfer, Newton's law is applied:

$$\frac{dQ_b}{dt}=Ah(T_s-T_e) \tag{14}$$

where Q_b represents the heat transfer (J), h is the heat transfer coefficient (W/m^2 K), A is the heat transfer surface area (m^2), T_s is the surface temperature of the solid (K), and T_e is the ambient temperature (K).

The final phenomenon to be considered is thermal radiation, which is modelled using the Stefan–Boltzmann law:

$$\frac{dQ_r}{dt}=\varepsilon\sigma\left(T_s^4-T_e^4\right)dS \tag{15}$$

where ε is the emissivity and σ is the Stefan–Boltzmann constant (W/m^2 K^4).

2.2. Network Model

A physical phenomenon that is modelled mathematically can be solved using the NSM. Each member of the mathematical model equation can be assigned an equivalent electrical element. In this case, we are dealing with a heat transfer problem which will have a corresponding electrical equivalent.

The equivalence between thermal and electrical variables has been extensively employed in heat transfer problems by Hao, L. et al. and Kreith, F. et al. [27,28]; however, the resolution methodology is different. Numerous engineering problems have been successfully solved through this method, as shown by Alhama, F. et al., Del Cerro Velázquez, F et al., Alhama, F. et al., Sánchez-Pérez, J.F. et al., and Solano, J. et al., [29–33].

To adapt Equation (14) for use with the NSM, we will express the term resulting from multiplying all summands on the left-hand side as thermal diffusivity, given its temperature-dependent variables. Additionally, through mathematical manipulation, the second derivative terms will be accomplished as two in-series resistors.

$$\frac{1}{r}\alpha\frac{\partial T}{\partial r}+\alpha\frac{\partial^2 T}{\partial r^2}+\alpha\frac{\partial^2 T}{\partial z^2}+\frac{Q}{\rho c_e}=\frac{\partial T}{\partial t} \tag{16}$$

To represent the second derivatives as resistors, it is compulsory to isolate them from variable terms. To achieve this, they are split into two components (Equation (18)). One component will be electrically analogous to a voltage-controlled current source, while the other will be represented by in-series-connected two resistors, as described by Fernández-García, M. et al. [26].

$$\alpha\frac{\partial^2 T}{\partial r^2}=(\alpha-1)\frac{\partial^2 T}{\partial r^2}+\frac{\partial^2 T}{\partial r^2} \tag{17}$$

For the $\frac{\partial^2 T}{\partial z^2}$ term, the same procedure is followed as for the $\frac{\partial^2 T}{\partial r^2}$ term, leaving Equation (16) as follows:

$$\frac{1}{r}\alpha\frac{\partial T}{\partial r}+(\alpha-1)\frac{\partial^2 T}{\partial r^2}+\frac{\partial^2 T}{\partial r^2}+(\alpha-1)\frac{\partial^2 T}{\partial z^2}+\frac{\partial^2 T}{\partial z^2}+\frac{Q}{\rho c_e}=\frac{\partial T}{\partial t} \tag{18}$$

Any second-order partial derivative without variable terms is represented in the circuit as in-series-connected two resistors. Similarly, any second-order or first-order partial derivative involving multiplicative dependent terms is represented as a voltage-controlled current source. Finally, the time derivative is represented as a capacitor. Consequently, our circuit will be configured as follows:

$\frac{1}{r}\alpha\frac{\partial T}{\partial r}$, $(\alpha-1)\frac{\partial^2 T}{\partial r^2}$, $(\alpha-1)\frac{\partial^2 T}{\partial z^2}+\frac{Q}{\rho c_e}$: some voltage-controlled current sources

$\frac{\partial^2 T}{\partial r^2}$, $\frac{\partial^2 T}{\partial z^2}$: two in-series-connected resistors; and $\frac{\partial T}{\partial t}$: one capacitor.

Given the temperature-dependent nature of the involved terms, voltage-controlled sources will be employed. Before applying the NSM, the differential equations are spatially discretised by splitting the space into n-volume elements, as depicted in Figure 3. This discretisation allows for the representation of the equations in finite difference form. Ultimately, the balance of currents at the centre of each cell is ensured by the electrical elements constituting the electrical circuit.

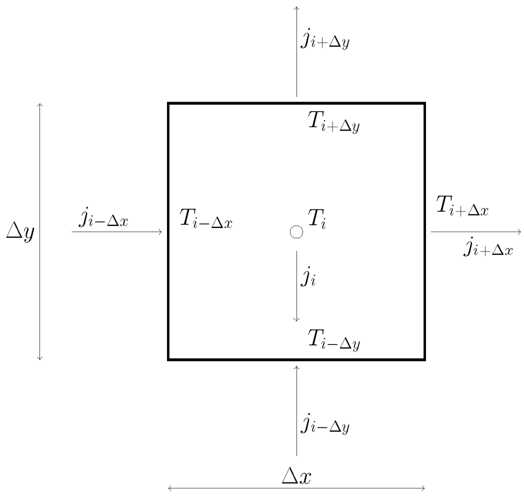

Figure 3. Volume element terminology.

Employing the terminology presented in Figure 3, the spatial discretisation of first and second derivatives is achieved through equilibrium considerations between central nodes and cell edges, as described by Kreith, F. and Zheng, W. et al. [28,34]. For instance, the finite difference approximation of the first derivative is given by:

$$\frac{\partial T}{\partial r} = \frac{T_{i+1,\,j} - T_{i-1,\,j}}{\Delta r} \tag{19}$$

where $\Delta r = r_{i+1,\,j} - r_{i-1,\,j}$, and the second derivative is:

$$\frac{\partial^2 T}{\partial r^2} = \frac{T_{i+1,\,j} + T_{i-1,\,j} - 2T_{i-1,\,j}}{\frac{\Delta^2 r}{2}} \tag{20}$$

In Equation (20) the value of the equivalent resistance for each node, R_z, when implementing the electrical element is:

$$R_{z,l} = \frac{1}{\frac{\Delta^2 r}{2}} \quad R_{z,r} = \frac{1}{\frac{\Delta^2 r}{2}} \quad R_{z,d} = \frac{1}{\frac{\Delta^2 z}{2}} \quad R_{z,u} = \frac{1}{\frac{\Delta^2 z}{2}} \tag{21}$$

Consequently, the circuit representing our problem, incorporating all the previously discussed elements, is illustrated in Figure 4. Each of the circuits in Figure 4a represents the unit cell defined in the geometry section. The boundary conditions, radiation, convection and spark gap effects are implemented by voltage-controlled current sources. The remaining voltage-controlled current sources represent the variation of the density variation, Figure 4b, the variation in the thermal conductivity, Figure 4c, the variation of the specific heat capacity, Figure 4d, and the variation in the thermal diffusivity, Figure 4e.

The network model is then solved by employing the circuit simulation program NGSpice, Holger, V. [35].

NGSpice (version ngspice-42), Holger, V. [35], employs computational algorithms to solve circuits understood from coupled and non-linear mathematical models, such as the one proposed in this article. These algorithms, rooted in the work of Nagel, L.W. [18,19], include Gear's time-stepping methods, Gear, C. W. [36], and trapezoidal integration, Nagel, L. [19]. Efficiency and accuracy are achieved by minimising local truncation errors and promoting stability in the numerical solution convergence [37].

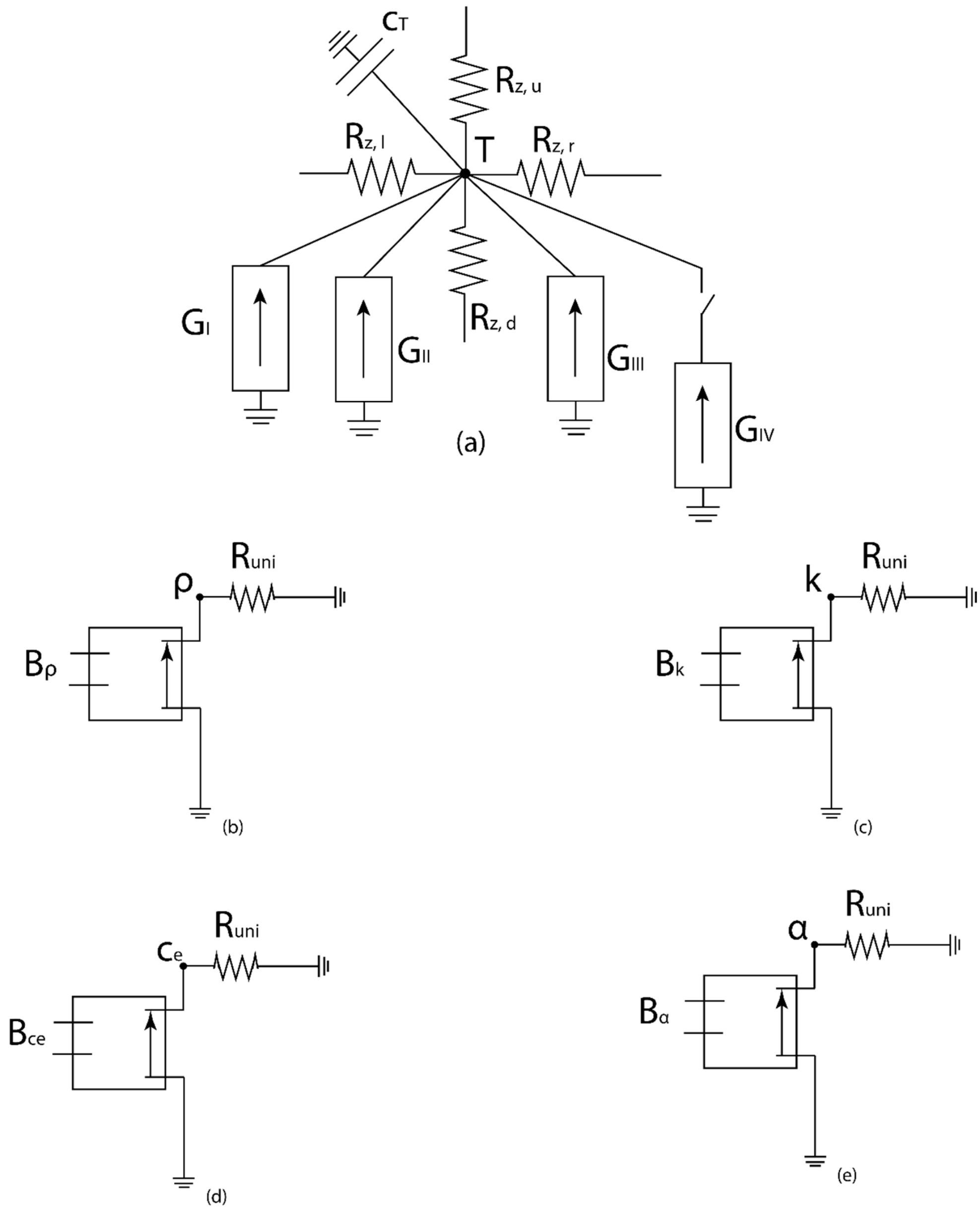

Figure 4. Volume element network model. (**a**) Temperature, (**b**) density, (**c**) thermal conductivity, (**d**) specific heat capacity, and (**e**) thermal diffusivity.

The novelty in the present work lies in the modelling of the spark application by implementing the discharge of a current source controlled by a switch; in Figure 4a, it can be seen that the G_{IV} source corresponds to the spark generator. This switch, when closed, discharges the source at the set time. Table 3 shows the different spark application times, which correspond to the time the switch remains closed. After the set time has elapsed, the switch opens, simulating the completion of the spark.

The section that makes up the optical fiber has also been simplified to include the core, the sheath, the protective layer and the metal where the spark is initiated. This reduction of the domain allows for reduced computational time, as the mesh is smaller.

Table 3. Temperature rise rate values for each simulation in r_T (K/s).

t (s)	P (W)	r_{T1} (K/s)	r_{T2} (K/s)	r_{T3} (K/s)	r_{T4} (K/s)
1	1	3816	3307	2928	2152
0.1	1	3816	3307	2928	2152
0.001	1	3816	3307	2928	2152
1	0.01	38.16	33.07	29.28	21.52
1	0.001	3.816	3.307	2.928	2.152
0.001	0.001	3.816	3.307	2.928	2.152

2.3. Nondimensionalization

Nondimensionalisation is a technique that requires a deep knowledge of the problem and a well-defined set of equations that represent the problem under study. The difference between this work and some previous ones lies in the importance of Q, which, in this problem, initiates the temperature change in the system. Thus, its importance with respect to the rest of the variables is studied. The difference is that this article has to be customised and take into account the Q energy source.

The following is a brief explanation of the procedure to be followed in order to apply this technique. Firstly, the dimensionless variables are established, which are as follows:

$$Q' = \frac{Q}{Q_{max}};\ t' = \frac{t}{\tau};\ T' = \frac{T - T_i}{T_e - T_i}\ ;\ r' = \frac{r}{R}\ ;\ z' = \frac{z}{H} \tag{22}$$

where Q_{max} is the maximum power obtained, T_i is the initial temperature, T_e is the ambient temperature, H is the height, and τ is the steady state time and R is the radius.

Applying the $\pi - theorem$, we obtain the following dimensionless numbers:

$$\pi_1 = \frac{\alpha\tau}{R^2}\ ;\ \pi_2 = \frac{R^2}{H^2}\ ;\ \pi_3 = \frac{\alpha h\tau}{Rk}\ ; \pi_4 = \frac{hR}{k} \tag{23}$$

Here, π_1 represents the temperature change associated with diffusion phenomena, while π_2 represents the cylinder's dimensions geometric relationship. π_3 predominates in convection phenomena. π_4 = hD/k, where D is the cylinder diameter. This is the Nusselt number, Nu, which describes the heat transfer coefficient, h, and the thermal conductivity of the material, k [27].

$$\pi_5 = \frac{Q_{max}R^2}{k} \tag{24}$$

π_5 relates the maximum rate of temperature rise to the driving effects. As can be seen, the effect of Q on heat transfer in the system depends, logically, on geometrical factors, R, which in turn is related to H through π_1, π_2 and on the thermal conductivity, k, which in turn is related to density and c_p through π_1, since all of them are included in α. Finally, the time to reach steady state, is obtained with τ :

$$\tau = \frac{R^2}{\alpha} f\left(\frac{R^2}{H^2}, \frac{Q_{max}R^2}{k}, \frac{hR}{k}\right) \tag{25}$$

where f is an unknown function. From Equation (25) it follows that the steady state depends on the heat generated by the fiber melting effect, the geometry of the optical fiber and the conductivity of the material.

3. Results

In Figures 5–10, the same process is represented, with equal spark application time and equal power, but for the four different cases that can be seen in Table 1. Thus, section (a) corresponds to case 1 and is the one with the smallest area and index n_1. Section

(b) corresponds to case 2, section (c) to case 3 and section (d) is for the last case, 4, which has the largest area and the highest index n_1.

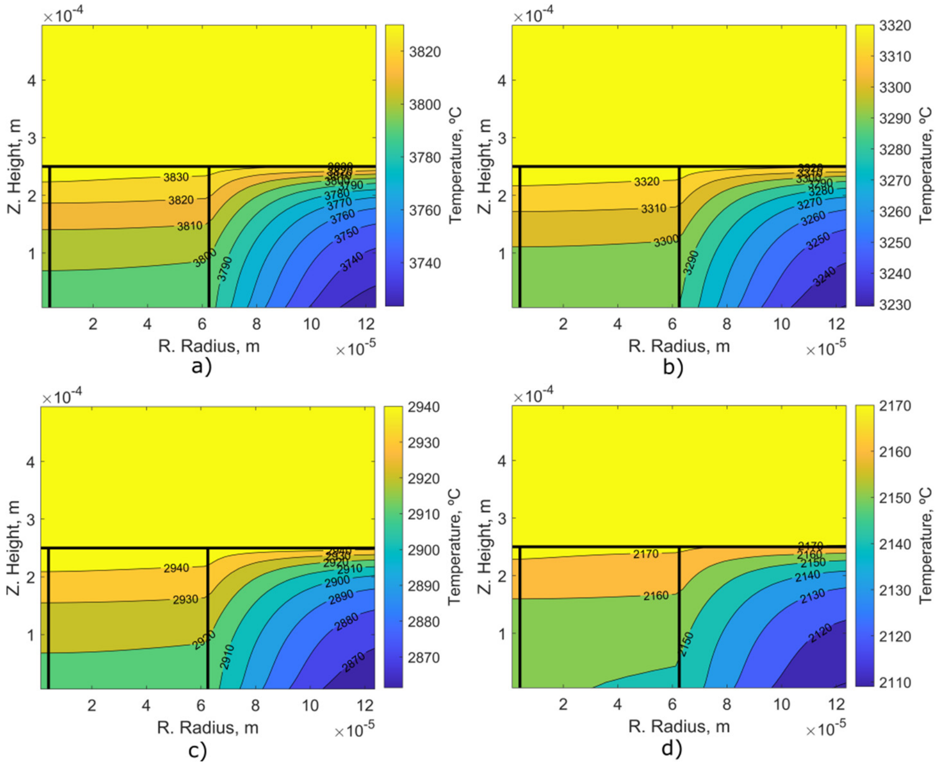

Figure 5. Results for the 4 cases with a spark application time of 1 s. Case 1 (**a**), Case2 (**b**), Case 3 (**c**) and Case 4 (**d**).

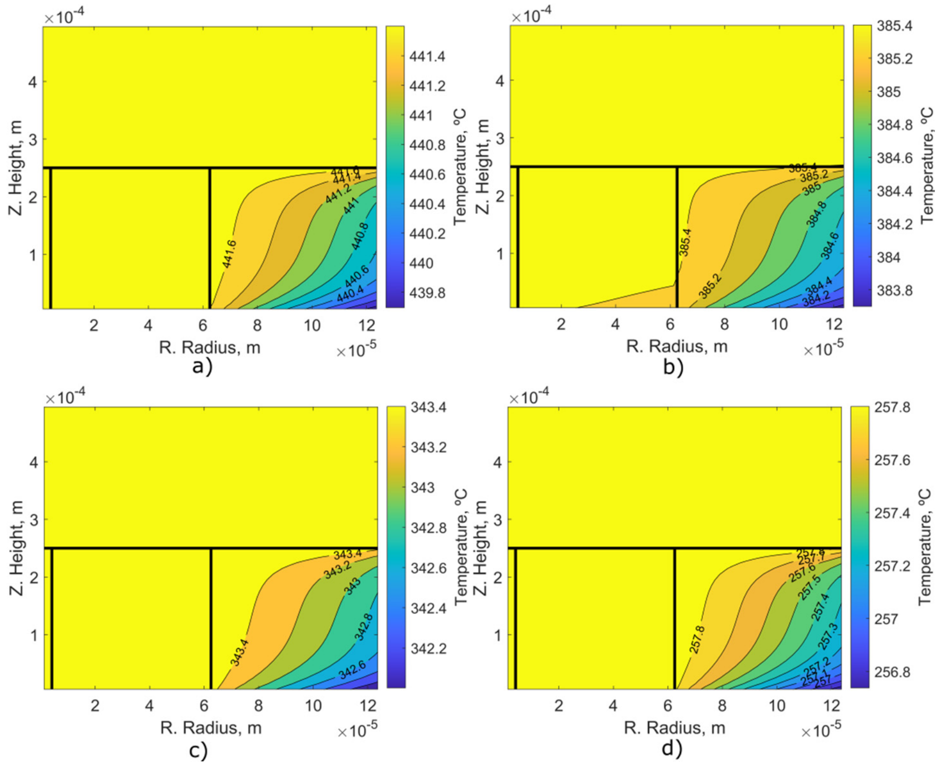

Figure 6. Results for the 4 cases with a spark application time of 0.1 s. Case 1 (**a**), Case2 (**b**), Case 3 (**c**) and Case 4 (**d**).

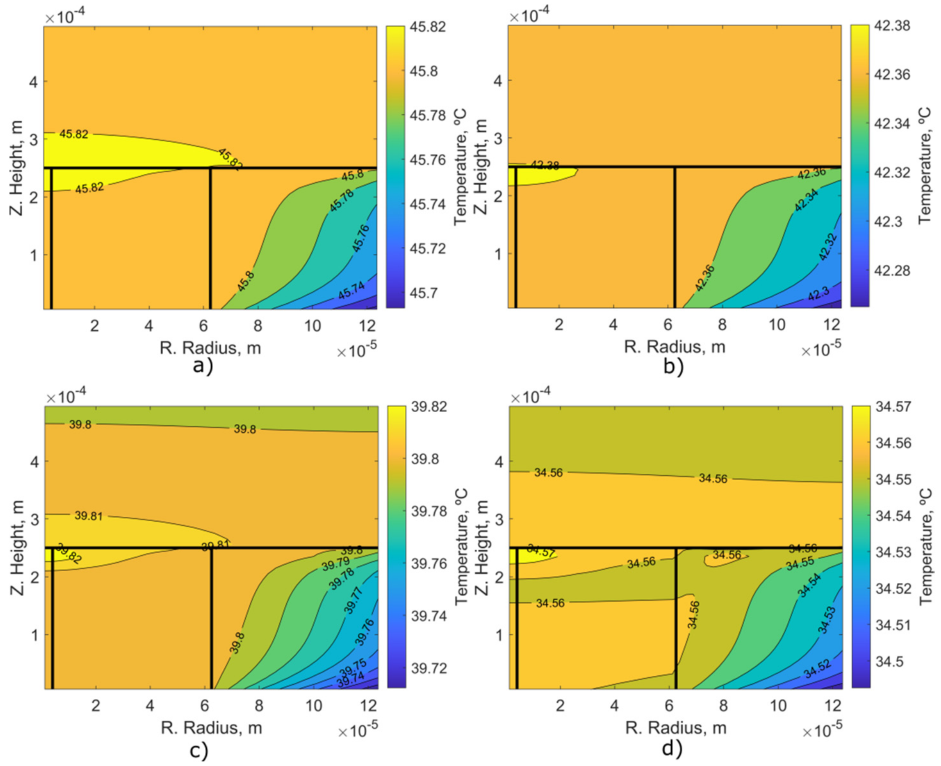

Figure 7. Results for the 4 cases with a spark application time of 1 ms. Case 1 (**a**), Case2 (**b**), Case 3 (**c**) and Case 4 (**d**).

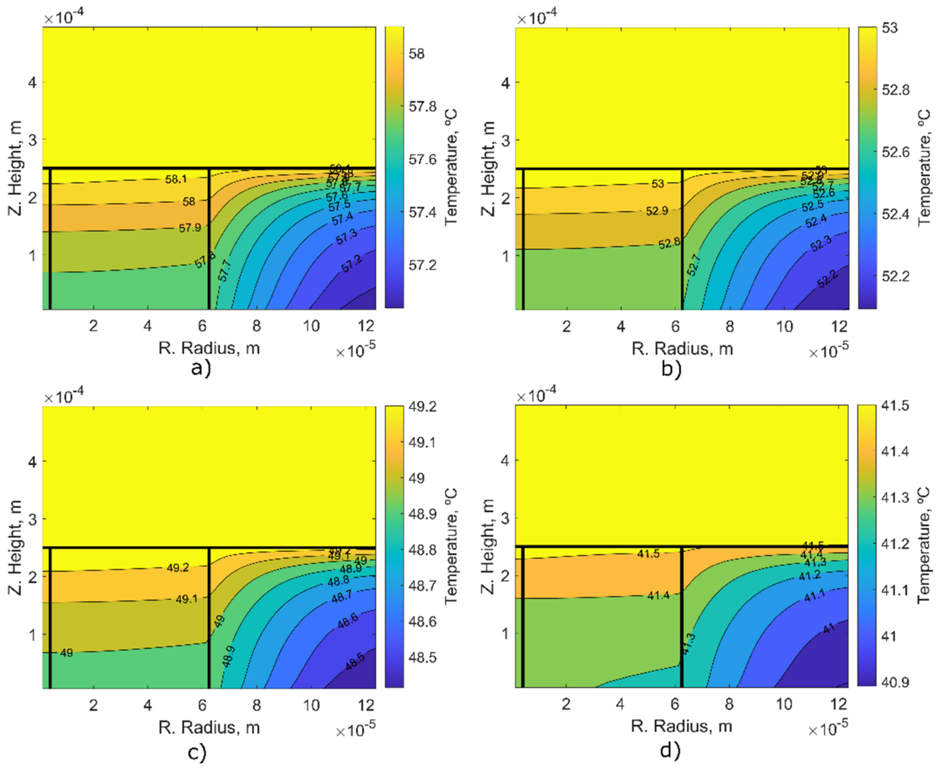

Figure 8. Results for the 4 cases with a spark application time of 1 s and power of 10 mW. Case 1 (**a**), Case2 (**b**), Case 3 (**c**) and Case 4 (**d**).

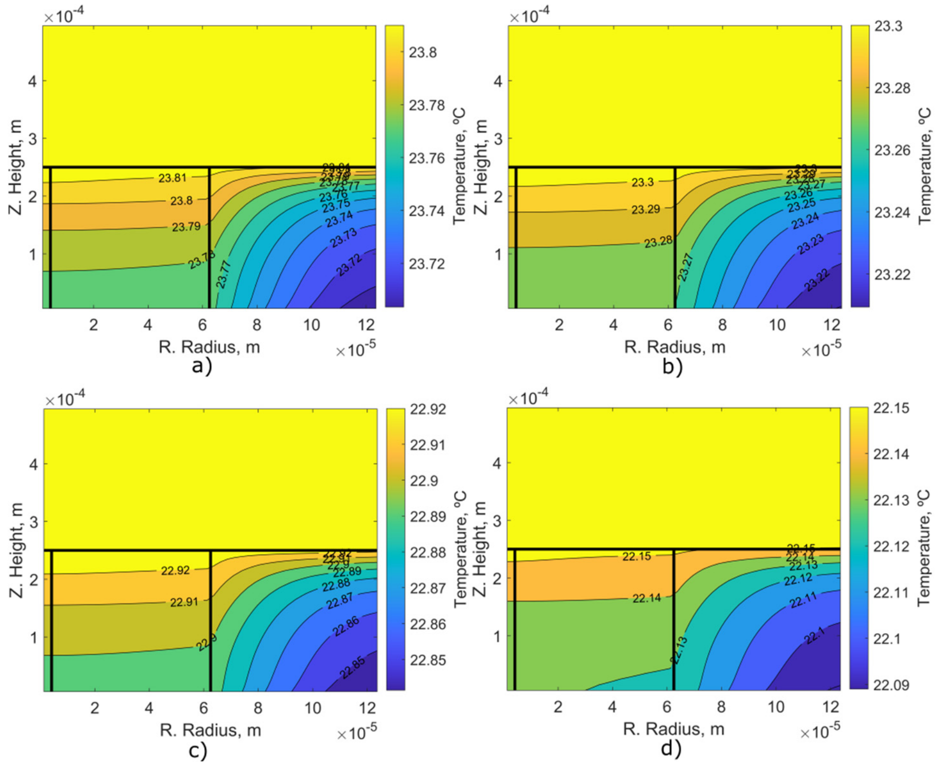

Figure 9. Results for the 4 cases with a spark application time of 1 s and power of 1 mW. Case 1 (**a**), Case2 (**b**), Case 3 (**c**) and Case 4 (**d**).

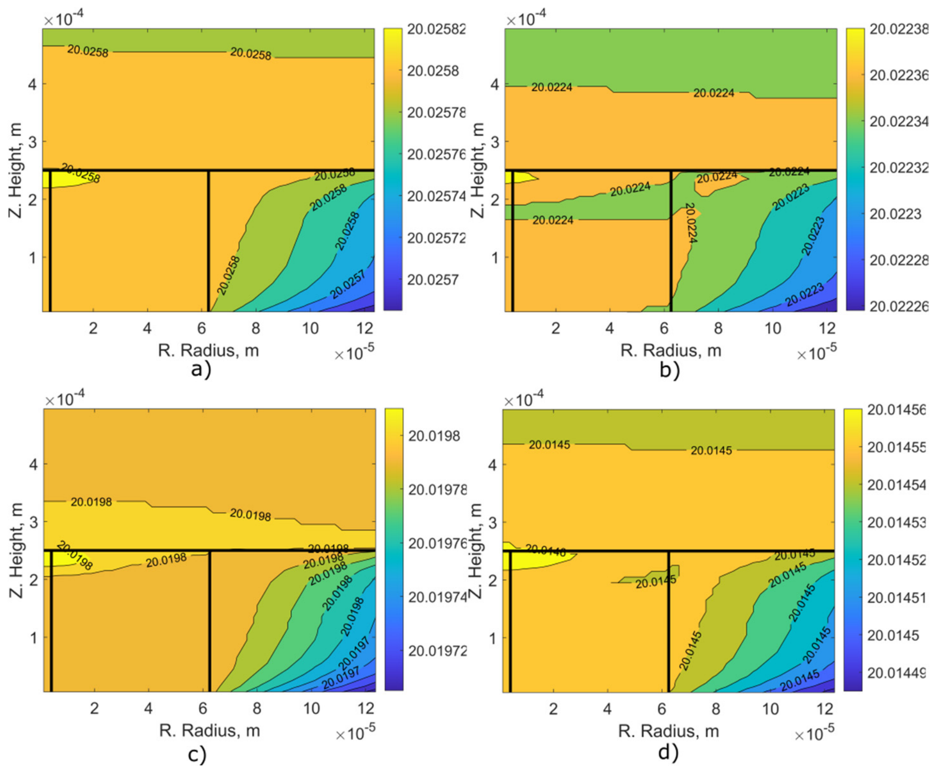

Figure 10. Results for the 4 cases with a spark application time of 1 ms and power of 1 mW. Case 1 (**a**), Case2 (**b**), Case 3 (**c**) and Case 4 (**d**).

This section can be organised into subheadings. It should provide a clear and concise summary of the experimental findings, their interpretation, and the resulting experimental conclusions.

In Figure 5, the temperature rise speed corresponding to r_T to the $\frac{Q}{\rho c_e}$ term in Equation (10) is higher in section (a) and the lowest in section (d). Due to the cross-section of the optical fiber, which is smaller in section (a), the generation of energy is greater in less surface area, so the temperature rise speed is higher than in the rest of the cases. On the other hand, in case 4, which has the largest cross-section, the rate of rise is the lowest since the larger cross-section means that the energy dissipation is greater.

Table 3 shows the different values obtained by NSM of r_T (K/s) for different spark application times, t (s), and applied power, P (W). The simulation time is always 1 s, and t is the application time of Q.

The behaviour of the problem in Figures 6–10 is similar to that described in Figure 5. It is clear that the temperature reached is conditioned by the time of application of the spark and the power of the spark. Figure 6 shows that with the reduction of the time from 1 s (Figure 5) to 0.1 s (Figure 6), the temperature reached is lower than that reached by applying the spark for 1s.

Next, a study of the variables of the problem will be carried out using the expression obtained by means of nondimensionalization. Substituting the value of α into expression (25) gives Equation (26). As can be seen, the variables that only appear in a monomial are the specific heat capacity, c_e, density, ρ, heat transfer coefficient, h, and maximum heat transfer.

$$\tau = \frac{\rho c_e R^2}{k} f\left(\frac{R^2}{H^2}, \frac{Q_{max} R^2}{k}, \frac{hR}{k}\right) \tag{26}$$

In this work, the effect of material density on heat transfer with a spark application time of 1 s and power of 1 W will be studied. Table 4 and Figure 11 show the results obtained from the study, where it can be seen how the effect of this variable on temperature is studied at two points with different materials, cladding and the guard envelope. The position for T_1, cladding, is ($6.25 \cdot 10^{-5}$, $1.25 \cdot 10^{-4}$) m, and for T_2, guard envelope, is ($12.37 \cdot 10^{-5}$, $1.25 \cdot 10^{-4}$) m. Thus, the effect of variations with respect to a base case is studied. For case 1, the value of the fibre density is halved so that, as shown in expression (26), the simulation time must be halved to obtain the same temperature value in 1. However, since the value of the density of the envelope guard is not also halved, the value in 2 must be different. For case 2, only the value of the guard envelope density is halved, and the simulation time of the base case is maintained, so as expected the value of T_1 is the same and T_2 is not, as it is influenced by the heat transmission from the fibre. Finally, in case 3, both densities are halved, so according to expression (26), the simulation time must also be halved. In this case, by halving both densities, in contrast to case 1, the same temperature values are obtained as in the base case.

Table 4. Study of the density of materials.

Case	ρ_{Fiber} (kg/m^3)	ρ_{guard} (kg/m^3)	t (s)	T_1 (°C)	T_2 (°C)
Base	2220	1190	1	3804	3743
1	1110	1190	0.5	3804	3690
2	2220	595	1	3804	3770
3	1110	595	0.5	3804	3743

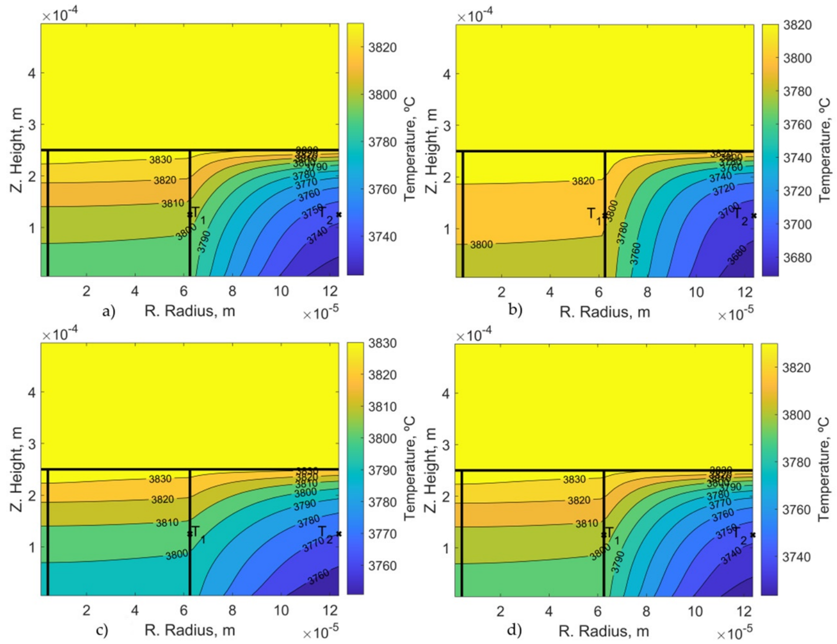

Figure 11. Results for the 4 cases with a spark application time of 1 s and power of 1 W. Base (**a**), Case 1 (**b**), Case 2 (**c**) and Case 3 (**d**). See Table 4.

4. Discussion

Table 3 shows that the r_{Ti} remain constant as long as the applied power does not vary. As the power decreases, the rate of rise does vary, and this variation is of the same factor as the power decrease factor.

A strong dependence can be established between the rate of rise, the characteristics of the section and the applied power.

These results obtained in the simulation agree with the analysis of the behaviour of the equations and parameters governing the fiber optic fusion process.

Through nondimensionalization, it has been possible to establish which variables are relevant and which variables are superfluous, as seen in the Results section. It has been possible to reduce the number of variables that intervene or have a significant weight in the problem.

Thus, the factor α_e has a value of $\alpha_e \approx 8.888{\cdot}10^{-11}\ \mathrm{m}^{-1}$ which makes its influence practically negligible and the factor $\alpha(r,\ z) = \alpha_0 + \alpha_e \approx \alpha_0 = 1\ \mathrm{m}^{-1}$. The gamma function, $\Gamma(\mathrm{x}) = \frac{1}{\sqrt{2\pi}} e^{-\frac{x^2}{2}} = 0.159$, is a constant value. With this it can be seen how the heat generated and the rate of rise only relies on the applied power and the effective area of the optical fiber, $Q(r,z) = \alpha(r,\ z)\frac{P}{A_{eff}}\Gamma(r,z) = 0.159\ \frac{P}{A_{eff}}$. With this result, it can be assured that the simulations present results in agreement with the analysis of the equations.

5. Conclusions

In this work, we have studied the phenomenon of optical fiber fusion by plasma spark. A methodology has been developed in NSM that has allowed us to design a circuit with the same behaviour as the physical process. One aspect to highlight is the control that we have been able to carry out on the time and application of the spark, as well as the applied power; this has allowed us to check the effect that each of these terms has, reaching the conclusion that the parameter that most influences the rate of temperature rise is the power, as can be seen in Table 3.

In the analysis of the equations that govern the process (see Section 4 Discussion), it was found that most of the terms are either constant or their influence is negligible, leaving as main variables those that define the section, the material and the power of the spark.

The results obtained are used to study the behaviour of different materials with respect to the damage caused by the fusion of the optical fiber caused by a high-energy spark and to establish a power limit for each type of material that allows different protection devices to be designed according to the material selected.

It is interesting how the temperature varies depending on the material selected. This result leads to the selection of the most suitable materials for this defect, which has an impact on the design of better-quality fiber optic cables.

Author Contributions: Conceptualization, J.F.S.-P. and E.C.; methodology, J.F.S.-P., J.S.-R. and F.M.-G.; software, J.F.S.-P. and J.S.-R.; validation, J.F.S.-P., J.S.-R., E.C. and F.M.-G.; formal analysis, J.F.S.-P., J.S.-R., E.C. and F.M.-G.; writing—original draft preparation, J.F.S.-P., J.S.-R., E.C. and F.M.-G.; writing—review and editing, J.F.S.-P., J.S.-R., E.C. and F.M.-G. All authors have read and agreed to the published version of the manuscript.

Funding: This research received no external funding.

Data Availability Statement: The original contributions presented in this study are included in the article. Further inquiries can be directed to the corresponding author. The data presented in this study are available on request from the corresponding author.

Conflicts of Interest: The authors declare no conflicts of interest.

References

1. Kashyap, R. Self-propelled self-focusing damage in the optical fibres. In *Lasers 1987, Proceedings of the Tenth International Conference on Lasers and Applications, Lake Tahoe, NV, USA, 7–11 December 1987*; Duarte, F.J., Ed.; STS Press: McLean, VA, USA, 1988; pp. 859–866.
2. Kashyap, R.; Blow, K.J. Observation of catastrophic self-propelled self-focusing in optical fibres. *Electron. Lett.* **1988**, *24*, 47–49. [CrossRef]
3. Kashyap, R.; Sayles, A.H.; Cornwell, G.F. Heat-flow modeling and visualization of catastrophic self-propagating damage in single-mode optical fibers at low powers. In *Laser-Induced Damage in Optical Materials: 1996*; SPIE: Bellingham, WA, USA, 1997; pp. 586–591.
4. Starikova, V.A.; Konin, Y.A.; Petukhova, A.Y.; Aleshkina, S.S.; Petrov, A.A.; Perminov, A.V. Mathematical Model of Fuse Effect Initiation in Fiber Core. *Algorithms* **2023**, *16*, 331. [CrossRef]
5. Todoroki, S. *Fiber Fuse*; NIMS Series; Springer: Berlin/Heidelberg, Germany, 2014. [CrossRef]
6. Ha, W.; Jeong, Y.; Oh, K. Fiber fuse effect in hollow optical fibers. *Opt. Lett.* **2011**, *36*, 1536–1538. [CrossRef] [PubMed]
7. Shuto, Y. End Face Damage and Fiber Fuse Phenomena in Single-Mode Fiber-Optic Connectors. *J. Photonics* **2016**, *2016*, 2781392. [CrossRef]
8. Xiao, Q.; Tian, J.; Yan, P.; Li, D.; Gong, M. Exploring the initiation of fiber fuse. *Sci. Rep.* **2019**, *9*, 11655. [CrossRef]
9. Konin, Y.A.; Scherbakova, V.A.; Bulatov, M.I.; Malkov, N.A.; Lucenko, A.S.; Starikov, S.S.; Grachev, N.A.; Perminov, A.V.; Petrov, A.A. Structural characteristics of internal microcavities produced in optical fiber via the fuse effect. *J. Opt. Technol.* **2021**, *88*, 672–677. [CrossRef]
10. Shuto, Y. Fiber Fuse Simulation in Multi-Core Fibers for Space Division Multiplexed Transmission. *J. Electr. Electron. Eng.* **2022**, *10*, 162–169.
11. Lin, G.-R.; Baiad, M.D.; Gagne, M.; Liu, W.-F.; Kashyap, R. Harnessing the fiber fuse for sensing applications. *Opt. Express* **2014**, *22*, 8962. [CrossRef]
12. Mizuno, Y.; Lee, H.; Hayashi, N.; Nakamura, K.; Todoroki, S.-I. Plastic Optical Fiber Fuse and Its Impact on Sensing Applications. Available online: http://www.youtube.com/ (accessed on 20 November 2024).
13. Leal-Junior, A.G.; Marques, C.; Lee, H.; Nakamura, K.; Mizuno, Y. Sensing Applications of Polymer Optical Fiber Fuse. *Adv. Photonics Res.* **2022**, *3*, 2100210. [CrossRef]
14. Xiao, Q.; Tian, J.; Li, D.; Huang, Y.; Wang, Z.; Yan, P.; Gong, M. An Efficient Non-Invasive Method to Fabricate In-Fiber Microcavities Using a Continuous-Wave Laser. *IEEE Photonics Technol. Lett.* **2020**, *32*, 573–576. [CrossRef]

15. Tian, J.D.; Wang, Z.H.; Xiao, Q.R.; Li, D.; Yan, P.; Gong, M.L. On the initiation of fiber fuse damage in high-power ytterbium-doped fiber lasers. *Photonics Res.* **2022**, *10*, 2513–2525. [CrossRef]
16. Tian, J.D.; Xiao, Q.R.; Li, D.; Zhang, Z.; Yin, H.Y.; Yan, P.; Gong, M.L. Fiber Fuse Damage Effect in Fiber Lasers: A Review. *Chin. J. Lasers-Zhongguo Jiguang* **2021**, *48*, 81–105.
17. Peusner, L. *The Principles of Network Thermodynamics: Theory and Biophysical Applications*; Entropy Limited: Amador, CA, USA, 1987.
18. Nagel, L. SPICE (Simulation Program with Integrated Circuit Emphasis). In Proceedings of the 16th Midwest Symposium on Circuit Theory, Waterloo, ON, Canada, 12 April 1973.
19. Nagel, L.W. *SPICE2: A Computer Program to Simulate Semiconductor Circuits*; College of Engineering, University of California: Berkeley, CA, USA, 1975.
20. Sánchez-Pérez, J.F.; Alhama, I. Universal curves for the solution of chlorides penetration in reinforced concrete, water-saturated structures with bound chloride. *Commun. Nonlinear Sci. Numer. Simul.* **2020**, *84*, 105201. [CrossRef]
21. Carslow, H.S.; Jaeger, J.C.; Morral, J.E. Conduction of heat in solids. *J. Eng. Mater. Technol.* **1986**, *108*, 378. [CrossRef]
22. Davis, D.D., Jr.; Mettler, S.C.; DiGiovanni, D.J. Experimental data on the fiber fuse. In Proceedings of the 27th Annual Boulder Damage Symposium: Laser-Induced Damage in Optical Materials, Boulder, CO, USA, 30 October–1 November 1995; SPIE: Bellingham, WA, USA, 1996; pp. 202–210.
23. Hanafusa, H.; Hibino, Y.; Yamamoto, F. Formation mechanism of drawing-induced E' centers in silica optical fibers. *J. Appl. Phys.* **1985**, *58*, 1356–1361. [CrossRef]
24. Shuto, Y.; Yanagi, S.; Asakawa, S.; Kobayashi, M.; Nagase, R. Fiber fuse phenomenon in step-index single-mode optical fibers. *IEEE J. Quantum Electron.* **2004**, *40*, 1113–1121. [CrossRef]
25. Marcuse, D. Loss analysis of single-mode fiber splices. *Bell Syst. Tech. J.* **1977**, *56*, 703–718. [CrossRef]
26. Hao, L.; Xu, F.; Chen, Q.; Wei, M.; Chen, L.; Min, Y. A thermal-electrical analogy transient model of district heating pipelines for integrated analysis of thermal and power systems. *Appl. Therm. Eng.* **2018**, *139*, 213–221. [CrossRef]
27. Kreith, F.; Bohn, M.S. *Principles of Heat Transfer*; Harper and Row Publishers Inc.: New York, NY, USA, 1986.
28. Alhama, F.; Campo, A. Electric Network Representation of the Unsteady Cooling of a Lumped Body by Nonlinear Heat Transfer Modes. *J. Heat Transf.* **2002**, *124*, 988–992. [CrossRef]
29. Del Cerro Velázquez, F.; Gómez-Lopera, S.A.; Alhama, F. A powerful and versatile educational software to simulate transient heat transfer processes in simple fins. *Comput. Appl. Eng. Educ.* **2008**, *16*, 72–82. [CrossRef]
30. Alhama, F.; González-Fernández, C.F. Network simulation method for solving phase-change heat transfer problems with variable thermal properties. *Heat Mass Transf.* **2002**, *38*, 327–335. [CrossRef]
31. Sánchez-Pérez, J.F.; Marín, F.; Morales, J.L.; Cánovas, M.; Alhama, F. Modeling and simulation of different and representative engineering problems using Network Simulation Method. *PLoS ONE* **2018**, *13*, e0193828. [CrossRef]
32. Solano, J.; Balibrea, F.; Moreno, J.A.; Marín, F. Dry Friction Analysis in Doped Surface by Network Simulation Method. *Mathematics* **2023**, *11*, 1341. [CrossRef]
33. Fernández-Gracía, M.; Sánchez-Pérez, J.F.; del Cerro, F.; Conesa, M. Mathematical Model to Calculate Heat Transfer in Cylindrical Vessels with Temperature-Dependent Materials. *Axioms* **2023**, *12*, 335. [CrossRef]
34. Zheng, W.; Zhu, J.; Luo, Q. Distributed Dispatch of Integrated Electricity-Heat Systems with Variable Mass Flow. *IEEE Trans. Smart Grid* **2023**, *14*, 1907–1919. [CrossRef]
35. Holger, V.; Atkinson, G.; Nenzi, P.; Warning, D. Software "NgSpice". Available online: https://ngspice.sourceforge.io/index.html (accessed on 20 November 2024).
36. Gear, C.W. The automatic integration of ordinary differential equations. *Commun. ACM* **1971**, *14*, 176–179. [CrossRef]
37. Solano, J.; Mulas-Pérez, J.; Balibrea, F.; Moreno-Nicolás, J.A. Truncation Error of the Network Simulation Method: Chaotic Dynamical Systems in Mechanical Engineering. *Mathematics* **2024**, *12*, 3441. [CrossRef]